Correction of phase errors due to leakage currents in wideband EIT field measurements on soil and sediments

To cite this article: E Zimmermann *et al* 2019 *Meas. Sci. Technol.* **30** 084002

View the article online for updates and enhancements.

Correction of phase errors due to leakage currents in wideband EIT field measurements on soil and sediments

E Zimmermann[1] , J A Huisman[2] , A Mester[1] and S van Waasen[1,3]

[1] Central Institute for Engineering, Electronics and Analytics, Electronic Systems (ZEA-2), Forschungszentrum Jülich GmbH, Jülich, Germany
[2] Institute of Bio- and Geosciences, Agrosphere (IBG-3), Forschungszentrum Jülich GmbH, Jülich, Germany
[3] Faculty of Engineering, Communication Systems, University of Duisburg-Essen, Duisburg, Germany

E-mail: e.zimmermann@fz-juelich.de

CrossMark

Abstract

Electrical impedance tomography (EIT) is a promising method to characterize important hydrological properties of soil, sediments, and rocks. The characterization is based on the analysis of the phase response of the complex electrical conductivity in a broad frequency range (i.e. mHz to kHz). However, it is challenging to measure the small phase response of low-polarizable soils and rocks in the higher frequency range up to 10 kHz. In order to achieve the required phase accuracy in the kHz frequency range, an optimized measurement system and advanced model-based processing methods have been developed. Recently, EIT measurements at sites with low electrical conductivity have shown a new dominating phase error related to capacitive leakage currents between cable shields and soil. In order to correct this phase error, we developed an advanced finite element model that considers both leakage currents and capacitive coupling between the soil and the cable shields in the reconstruction of the complex electrical conductivity distribution. This advanced model also takes into account potential measurement errors due to high electrode impedances. The use of this advanced model reduced the new dominating error for media with low electrical conductivity. It was also found that the amount of leakage current is an additional indicator for data quality that can be used for data filtering. After application of a novel data filter based on the leakage current and the use of the advanced modelling approach, the phase error of the measured transfer impedances above 100 Hz was significantly reduced by a factor of 6 or more at 10 kHz. In addition, physically implausible positive phase values were effectively eliminated. The new correction method now enables the reconstruction of the complex electrical conductivity for frequencies up to 10 kHz at field sites with a low electrical conductivity.

Keywords: impedance spectroscopy, inductive coupling, capacitive coupling, leakage current, electrical impedance tomography

(Some figures may appear in colour only in the online journal)

1. Introduction

Imaging of the complex electrical conductivity inside objects is of interest in a broad range of research fields, including process tomography, medicine, and geophysics. In the simplest case, the complex electrical conductivity can be determined using two electrodes to supply a current to an object and two other electrodes to measure the electrical potential at the surface of the object. In order to achieve the highest possible image resolution, these measurements are repeated with many different electrode pairs on many different locations on the surface of the object. From the data thus measured, the electrical conductivity inside the object can be reconstructed using an inversion method.

Unfortunately, there is no consensus in the naming of this imaging method across different research fields. In process tomography, the name electric tomography is used as an umbrella term for the measurement of the electrical conductivity (real part), the dielectric permittivity or the magnetic permeability (York *et al* 2011). Typically, these measurements are used for process monitoring on pipes or columns. In medical applications, the method is called electrical impedance tomography (EIT) regardless of whether only the real part or the complex electrical conductivity is evaluated. An overview of initial developments in medical applications can be found in Barber and Brown (1984) and Yorkey *et al* (1987), and more recent developments are presented in Brown (2003), Holder (2005), Leonhardt and Lachmann (2012) and Frerichs *et al* (2017). In geophysics, this imaging approach is called electrical resistivity tomography (ERT) if the real part of the conductivity is measured at one frequency and induced polarization (IP), spectral induced polarization (SIP) or EIT if the complex electrical conductivity is measured at a few selected frequencies (IP) or a broad range of frequencies (SIP). An overview about the ERT method and geophysical applications can be found in Daily *et al* (2005). The IP effect can either be measured in the time domain or in the frequency domain. In time domain IP, the ground is polarized with a current and the polarization decay curve is measured after switching off the current. Bertin and Loeb (1976) and Sumner (1976) provide overviews of early IP metrology and its geophysical applications. In frequency domain IP, a series of sinusoidal excitation signals with different frequencies is injected and the amplitude and phase of the resulting voltages is measured. This method is used for example in the SIP measurements presented in Slater (2007), Kemna *et al* (2012) and Revil *et al* (2012b). SIP measurements with a single four-point electrode configuration with two excitation electrodes and two potential electrodes are methodologically equivalent to electrical impedance spectroscopy (EIS) measurements. Since this work is inspired by geophysical applications, we will rely on the terminology established in this field in the following.

The materials of interest in geophysical applications (e.g. soil and rock) typically are lossy dielectric media, and the electrical properties are therefore expressed as a complex electrical conductivity consisting of a real and imaginary part or a magnitude and a phase. The real part of the complex electrical conductivity is determined by ionic conduction in the pore space and the imaginary part of the complex electrical conductivity is determined by polarization processes associated with the electrical double layer at the interface between the soil matrix and the pore fluid (Börner *et al* 1996, Revil and Florsch 2010). Many previous field studies on complex electrical conductivity were limited to the lower frequency range of 0.1 Hz to 100 Hz (e.g. Kemna *et al* 2000, Williams *et al* 2009, Flores-Orozco *et al* 2011, 2012), mostly for technical reasons. However, new findings from laboratory and theoretical studies indicate that electrochemical polarization associated with small grains and pores in saturated and unsaturated porous media (Binley *et al* 2005b, Breede *et al* 2012), bacteria (Revil *et al* 2012), roots (Ozier-Lafontaine and Bajazet 2005), and nanoparticles (Joyce *et al* 2012, Flores-Orozco *et al* 2015) mainly affects the complex electrical conductivity in the kHz range. Therefore, there is a clear demand for the development of systems and methods for accurate spectral EIT measurements in the kHz frequency range in the field.

Due to the low polarizability of soils and rocks in the frequency range of interest with phase values between 0.1 and 20 mrad (Scott and Barker 2003, Binley *et al* 2005b) or the small amount of polarizable substances in the soil (nanoparticles, bacteria, roots), geophysical applications typically require a high phase accuracy of 1 mrad or better. Unfortunately, field measurements of such small phase angles in the frequency range up to 10 kHz are technically challenging because there is a range of error sources that affects the measurement accuracy and thus the resulting phase error (table 1).

An important source of errors is inductive coupling between the wires in multi-core cables. The significance of this coupling was already recognized by Pelton *et al* (1978a) and Telford *et al* (1990). Unfortunately, the bundling of electrical wires can hardly be avoided, especially in the case of borehole measurements where many electrodes are necessarily connected through a single cable bundle. In order to remove inductive coupling effects from borehole EIT measurements, correction methods have been developed based on a combination of calibration measurements and numerical modeling of the cable layout (Zhao *et al* 2013, 2015). Using this correction, a phase accuracy of 1 mrad at 1 kHz could be achieved when a custom-made measuring system optimized with respect to high phase accuracy was used (Zimmermann *et al* 2008, 2010).

Another source of electromagnetic coupling is the capacitive coupling between the current carrying and voltage measuring wires and between the wires and the soil, which can lead to capacitive crosstalk and parasitic leakage currents. Different methods are used to minimize the disturbing influence of capacitive coupling. In Dahlin and Leroux (2012), the coupling of unshielded wires is minimized by separating the wires for current excitation and voltage measurement into two separate branches. Another measure to avoid capacitive leakage currents and crosstalk between cables, especially if they are close together, is the use of shielded cables (Telford *et al* 1990). The use of shielded cables will strongly reduce the capacitive crosstalk, but the parasitic leakage currents between the cable shield and the soil remain. Zhao *et al* (2013) showed that this kind of coupling is of secondary importance

Table 1. Possible causes of phase errors in EIT measurements with surface electrodes.

Sources of error	Effect	Solution strategy	Reference
Inductive coupling between wires	Induces voltages in the voltage-measuring cables	Optimal cable layout and numerical corrections	Sunde (1968), Pelton *et al* (1978a), Zhao *et al* (2013, 2015)
Capacitive coupling between current carrying and voltage measuring unshielded wires	Capacitive crosstalk	Shielded cables	Telford *et al* (1990)
Capacitive coupling between current carrying unshielded wires and soil	Leakage current to soil	Shielded cables	Telford *et al* (1990)
Capacitive coupling between cable shield and soil	Leakage current from soil to shield	Content of this paper	
High contact impedance with capacitive load at the potential electrode	Phase shift at the electrodes	Content of this paper	

for borehole EIT measurements where the electrical conductivity is relatively high and the contact impedance between electrodes and the subsurface is low. However, Kelter *et al* (2018) observed unexpectedly high values for the imaginary part of the measured impedance for EIT measurements made with surface electrodes for dry soil conditions and associated high contact impedances between the electrodes and the subsurface. None of the corrections presented in Zhao *et al* (2013, 2015) could effectively reduce these observed large errors in the kHz frequency range. Furthermore, it was found that the capacitive leakage currents between the cable shields and the system ground were large compared to the current between the two excitation electrodes. These results suggest that the capacitive coupling for measurements in dry soil conditions is an important factor controlling the strength of the leakage current, and this has not been considered in sufficient detail in previous work.

High contact impedances at the potential electrodes also have an effect on the measurement accuracy of the complex electrical conductivity (Sumner 1976, Dahlin *et al* 2002, Binley and Kemna 2005a). The high impedances together with the capacitive load on the electrodes lead to phase errors in the potential measurements. This error can be minimized by measuring the potential directly at the electrode with high-impedance amplifiers (Zimmermann *et al* 2008). The remaining error can be corrected for four-electrode laboratory SIP measurements up to an error of 0.2 mrad for a frequency of 10 kHz with the methods outlined in Huisman *et al* (2016). For laboratory and field EIT measurements, the methods presented in Kelter *et al* (2015, 2018) can be used to reduce these errors to some extent. Nevertheless, a more advanced correction of the adverse effects of high contact impedances could further improve the accuracy of field EIT measurements.

The aim of this study is to compare field EIT measurements at two sites with low and high subsurface electrical conductivity and associated different contact impedances, and to present a novel error correction procedure to address measurement errors associated with capacitive coupling at test sites with low soil conductivity and high contact impedances. This correction procedure will include the determination of parasitic capacitances when measuring with surface electrodes

and the integration of these capacitances into the FEM model used for the reconstruction of the electrical conductivity distribution in EIT inversion. It is expected that this will also reduce errors due to high contact impedances. The correction procedure will also include the determination of leakage currents and an extended source term to correct the error due to the parasitic current flow from the subsurface via the cable shield to the system ground. The developed correction procedure will be verified using surface EIT measurements at the two field sites with low and high electrical soil conductivities for frequencies up to 10 kHz. It will also be investigated whether the EIT results improve when data are filtered based on the measured leakage current, because this seems an appropriate indicator of EIT data quality.

2. Methods

2.1. Measurement system

A custom-made 40-channel EIT measurement system was used for all EIT measurements presented here. It is based in large parts on the system described in Zimmermann *et al* (2008). The system is shown in figure 1 and consists of 40 electrode modules (EM01…EM40), 40 shielded electrode cables (EC01…EC40), a multiplexer unit (MUX), a function generator with a current measuring unit (FG) and a DAQ system (ADC) with 48 high-resolution analog to digital converters. For the broadband current excitation, two complementary sinusoidal voltage signals U_{i1} and U_{i2} are generated in the frequency range from 1 mHz to 45 kHz by the function generator. The two voltages are switched by the multiplexer unit to two freely selectable electrodes, eg. E01 and E40 in figure 1. The two excitation currents I_{m1} and I_{m2} are measured with two shunt resistors R_{s1} and R_{s2} in the signal path of the two complementary excitation voltages U_{i1} and U_{i2}. All remaining electrodes, E02 to E39 in figure 1, measure the voltages relative to system ground (GND) simultaneously to allow fast EIT measurements with a free choice of electrode configurations. For this purpose, the voltage signals are connected to the ADCs via the electrode modules, cables and multiplexers. The potential differences between electrodes
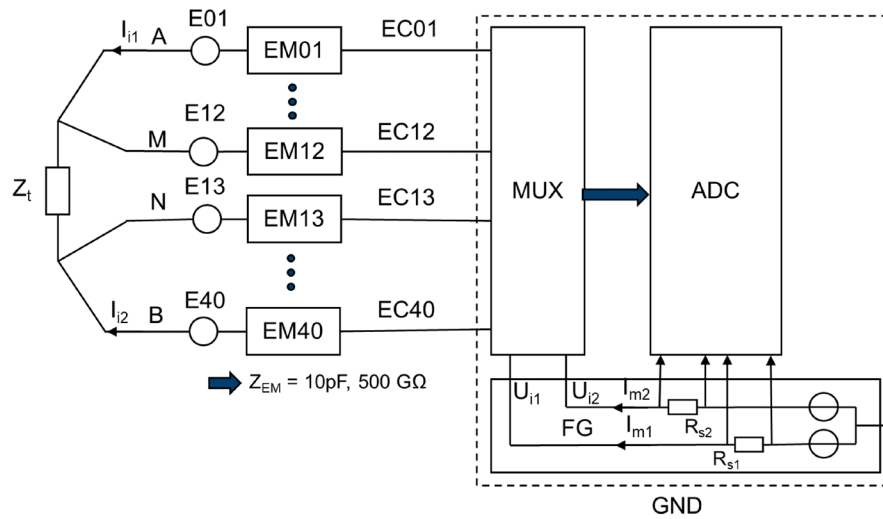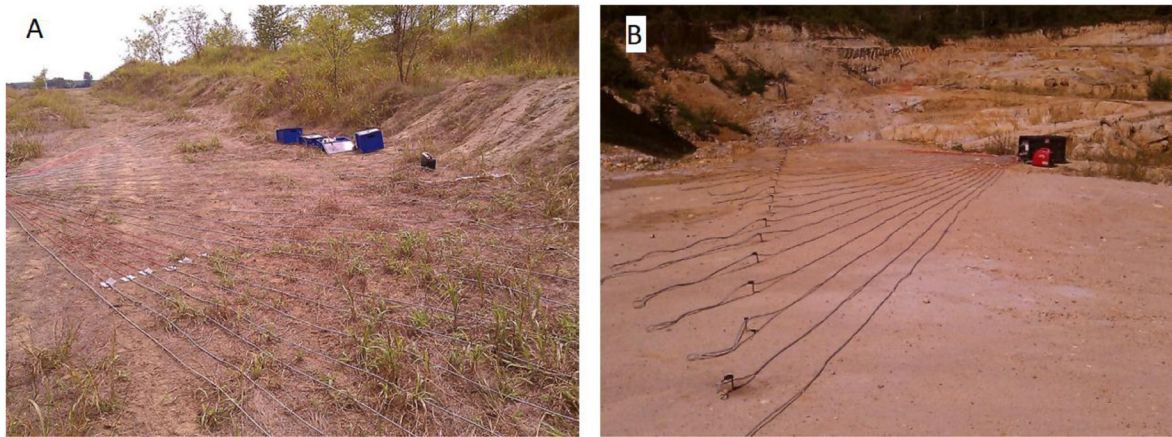
Figure 1. Block diagram of the EIT-system.

Figure 2. Location *A* with low soil electrical conductivity (<5 mS m^{-1}) near Senna Lodigiana, Italy (left) and location *B* with high soil electrical conductivity (>5 mS m^{-1}) near Lozzolo, Italy (right).

are calculated *a posteriori* for the four-point electrode configurations of interest. For example, the electrode configuration ABMN in figure 1 is calculated from the electrodes E01 and E40 for current injection and E12 and E13 for voltage measurements. In order to minimize the capacitive load at the electrodes, amplifiers for potential measurement and relays for switching off the inactive current channels are implemented in the electrode modules. The input impedance Z_{EM} of the electrode modules have an input capacitance of about 10 pF and an input resistance of about 500 GΩ.

In addition to the special system design, several error corrections are used to increase the measurement accuracy. In particular, correction methods have been developed to account for amplification errors, signal drift, current measurement errors, and propagation delay of the signal due to the long cables. To correct amplification errors that are mainly caused by the ADCs, a reference measurement with all channels is performed simultaneously on a single voltage source for the entire frequency range. The measured complex amplitudes of the voltages are stored as a calibration data set. To estimate the true currents at the electrodes (I_{i1} and I_{i2} in figure 1), the

transfer error of the current signals between measured currents I_{m1} and I_{m2} at the shunt resistors R_{s1} and R_{s2} and the electrodes E01... E40 are corrected numerically. For this purpose, the capacitive loads of the individual current paths from the shunt resistor to the individual electrodes, which consist of parts of the multiplexer and the cables, are measured. The propagation delay of the voltage signals from the electrode via the amplifiers to the ADCs is also corrected. More information about the system and the methods for error correction can be found in Zimmermann *et al* (2010).

2.2. Field EIT measurements

Field EIT measurements were conducted at two locations with different subsurface electrical conductivity. Both locations are located near Milano, Italy. Site *A* was located near Senna Lodigiana in the Lodi plain along a terrace of the Po river and showed a low electrical conductivity (figure 2(a)). Site *B* was located near Lozzolo and showed a higher electrical conductivity (figure 2(b)). More information about the two sites can be found in Inzoli (2016). At both sites, an array of
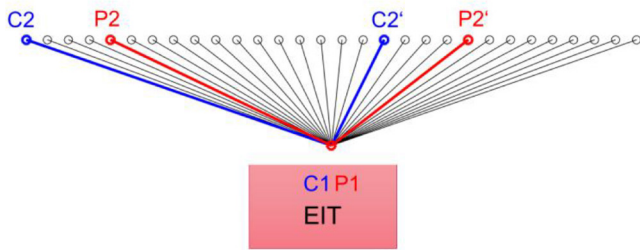
Figure 3. Schematic representation of the cable layout that allows straightforward calculation of the inductive coupling. This example shows the cable paths for two pole–pole configurations. For the first configuration, the cable paths are from C_1 to C_2 for the current-carrying cable and from P_1 to P_2 for the voltage-measuring cable. For the second configuration, the cable paths are from C_1 to C_2' and from P_1 to P_2'.

30 electrodes arranged in a row with an electrode spacing of 1 m was used, which resulted in a total length of 29 m for the electrode layout. Stainless steel screws with a length of 18 cm and a diameter of 10 mm were screwed into the soil to a depth of 10 cm and used as electrodes.

The electrode configurations for EIT measurements were selected considering the following two aspects. First, the electrodes for current excitation were selected so that a maximum signal to noise ratio is achieved. Since the EIT system used in this study measures voltages at all electrodes except the two current electrodes, the current electrodes were selected such that strong signals were expected at all electrodes. To achieve this, a large and as equal as possible spacing between the current electrodes was selected for all configurations. Second, it is desirable to acquire a primary data set in which each electrode is used equally often. This can be achieved with a circulating dipole-dipole configuration, see for example Xu and Noel (1993). Based on these considerations, we used current excitations where 16 electrodes were skipped in between the electrodes. At the end of the electrode array, the method is continued using the modulo operation, e.g. 01-18; 18-05 … 14-01. Using this approach, each electrode is used exactly two times for current excitation. In order to suppress the disturbing effect of external parasitic excitation currents, each current configuration is additionally carried out with exchanged current excitation electrodes (Zimmermann 2008). The average of the normal and the reversed excitations is used in the remainder of the processing. In order to obtain a dataset with reciprocal measurements, all pairs of current excitation electrodes were also used as potential electrodes. Using this strategy, the final data set consisted of 405 normal and 405 reciprocal transfer impedances for a total of 810 impedance measurements. For each current configuration, the impedances are measured for 15 frequencies in the range from 0.1 Hz to 10 kHz: 0.10, 0.23, 0.52, 1.18, 2.68, 6.10, 13.9, 31.3, 71.4, 164, 366, 850, 1950, 4400, 10 000 Hz. The measurement time was 80 min for a data set with all configurations and all frequencies.

2.3. Inductive coupling

Zhao *et al* (2015) showed that inductive coupling can cause large phase errors in EIT measurements, and suggested that

the position of the cables must be known with an accuracy of some cm to correct this error. Therefore, a simple fan-shaped cable layout was used for the EIT measurements where each electrode cable is positioned in a straight line from the EIT system to the electrode. Cable lengths of 20 m, 15 m and 10 m were used for the connections. In order to avoid additional inductive coupling, the cable sections that were too long were continued as a parallel cable end close together behind the electrodes. The cable layout is shown in figures 2 and 3.

To calculate the inductive coupling between the cables of the fan-shape cable layout, the method of Zhao *et al* (2015) based on the Neumann integral (Sunde 1968) is used. To optimize the calculation, all possible mutual inductances M between one current-carrying cable and one voltage-measuring cable are calculated using:

$$M = \frac{\mu}{4\pi} \int_{C_1}^{C_2} \int_{P_1}^{P_2} \frac{\mathrm{d}\vec{s}\mathrm{d}\vec{S}}{r} \tag{1}$$

where μ is the permeability, s and S are line elements, and r is the distance between these line elements. The cable paths are from C_1 to C_2 for the current-carrying cable and from P_1 to P_2 for the voltage-measuring cable (figure 3). This procedure results in a symmetrical pole–pole matrix with the inductances M_{CP} where C and P indicate the electrode number:

$$\boldsymbol{M_{30 \times 30}} = \begin{pmatrix} M_{1,1} & \cdots & M_{1,30} \\ \vdots & \ddots & \vdots \\ M_{30,1} & \cdots & M_{30,30} \end{pmatrix}. \tag{2}$$

The mutual inductance of any four-point configuration ABMN with two current electrodes AB and two potential electrodes MN is calculated in a second step using the superpositioning principle:

$$M_{\mathrm{ABMN}} = (M_{\mathrm{AM}} - M_{\mathrm{BM}}) - (M_{\mathrm{AN}} - M_{\mathrm{BN}}). \tag{3}$$

For each measured transfer impedance Z, the mutual inductance is added to the impedance component Z_{S} coming from the soil:

$$Z = Z_{\mathrm{s}} + j\omega M. \tag{4}$$

Using this equation, the measured transfer impedance can be corrected for inductive coupling by subtracting the mutual inductance.

2.4. FEM model with capacitive coupling

Capacitive coupling between the ground and the shield of the electrode cables cannot be corrected *a priori* because it depends on the potential distribution in the subsurface. Therefore, capacitive coupling can only be considered by integrating the capacitances in the FEM model used for modelling and reconstruction of the complex electrical conductivity distribution. For this, the soil part $\boldsymbol{Y_S}$ in the admittance matrix of the FEM model is supplemented by an additional matrix $\boldsymbol{Y_C}$ that represents the capacitive coupling (Zhao *et al* 2013):

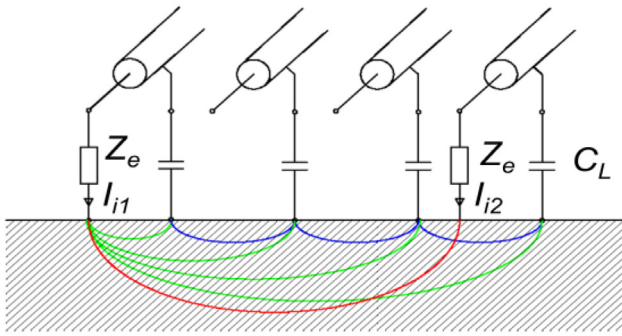$$[\boldsymbol{Y_G}] = [\boldsymbol{Y_S}] + [\boldsymbol{Y_C}]. \tag{5}$$

Figure 4. Schematic drawing illustrating capacitive coupling between soil and cable shield. I_i are the excitation currents, C_L the respective capacitances between soil and shield and Z_e the contact impedances of the current electrodes.

The matrix Y_C only has the elements $Y_{C_{n,n}}$ on the main diagonal

$$[Y_C] = \begin{bmatrix} Y_{C_{1,1}} & \cdots & 0 \\ \vdots & \ddots & \vdots \\ 0 & \cdots & Y_{C_{n,n}} \end{bmatrix} \quad (6)$$

which represent the capacitive connection at the nodes n of the FEM mesh to system ground (see figure 4). The FEM modeling itself is based on Poisson's equation (e.g. Pelton *et al* 1978b):

$$\nabla \cdot (\sigma \nabla \phi) = I\delta(r) \quad (7)$$

with the complex electric conductivity σ, the electric potential ϕ and the punctual current injection $I\,\delta(r)$.

The elements of the matrix Y_C must be determined from available information or additional measurements in order to not increase the number of unknowns in the solution of the inverse problem. Obviously, the cable position also needs to be known to specify the elements $Y_{C_{n,n}}$, but this is no additional effort because cable positions were already required for the inductive coupling. Unfortunately, it is difficult to determine the distance between cable shield and the surface in a field EIT measurement. Therefore, an analytical calculation of the individual capacitances as used in Zhao *et al* (2013, 2015) is not feasible. Instead, the total capacitance C_T between all cable shields and the ground is measured and distributed among the elements of Y_C according to the cable lengths and positions. In order to measure C_T, a current I_i is injected at one electrode and potential measurements U_P are performed at all other electrodes. C_T can then be calculated using:

$$j2\pi f C_T = \frac{I_i}{\text{mean}(U_p)} = \sum Y_{C_{n,n}} \quad (8)$$

where j is the imaginary unit, f is the measurement frequency and Σ is the sum operator. In this additional measurement, the resulting current flows from the current electrode through the soil and the cable shields back to the system. This is, for example, the green current path in figure 4 from the input point at I_{i1} to the capacitances of the cable shield. In this case, I_{i2} is zero. The imaginary part of the measured impedance between soil and system ground is essentially caused by the capacitance C_T. To increase the accuracy of the C_T estimate, the total

capacitance is measured by exciting at each electrode E01 to E30. The mean of all measured C_{Tn} is then used to calculate the mean total capacity C_T:

$$C_T = \text{mean}(C_{Tn}). \quad (9)$$

In addition to the capacitances between cable and ground, the input capacitances of the electrode modules are taken into account at the electrode positions in the FEM mesh.

Similar to Zhao *et al* (2013), the capacitances between the cable shield and the ground are distributed on the nodes of the affected elements in the FEM mesh. The cable paths are first divided into short segments of equal length. Next, the elements of the FEM mesh that have a triangular surface on the surface of the ground are identified. With a search algorithm, the cable segments are assigned to the individual triangular surface elements. The capacitance is determined for each element using the proportion of the cable segment and the cable length and added to the respective elements of Y_C. After all cable segments have been assigned, the sum of the elements $Y_{C_{n,n}}$ must match the measured total capacity.

To get a feeling for the plausibility of the measured total capacitance, the total capacitance was also estimated from an analytical solution for the capacity between a wire and a plate:

$$C = \frac{2\pi\varepsilon l}{a\cosh(d/R)} \quad (10)$$

with the permittivity ε, the total cable length l, the radius R of the wire, and the distance d between the wire axis and the plate. Assuming a total length $l = 380$ m for all cables, a radius $R = 2$ mm, a distance range of $d = 2.5$ mm to 10 mm, and the permittivity of air (8.85 pF m^{-1}), the total capacitance was expected to vary between 9.2 and 30.5 nF for the used cable lay-out.

2.5. FEM model with modified source term

Most EIT studies used a symmetric source term for the modelling of the current excitation (e.g. Binley and Kemna 2005a, Zimmermann *et al* 2008). Current flow to system ground is typically not considered. In this case, the inflowing and outflowing currents at the two excitation electrodes are identical. Although this simplification takes into account the current across parasitic parallel paths, this is only one part of the capacitive coupling effect. Therefore, it is necessary to modify the source term in order to consider the leakage current to the EIT system as well.

The schematic diagram in figure 4 is used to explain the current paths for a two-point excitation with capacitive coupling between cable shields and ground. The red path is the symmetric part I_S of the two excitation currents I_{i1} and I_{i2} and the green paths are possible leakage currents I_L to the cable shields. In order to calculate the effect of leakage currents on the measured transfer impedance, the excitation I is decomposed into two parts:

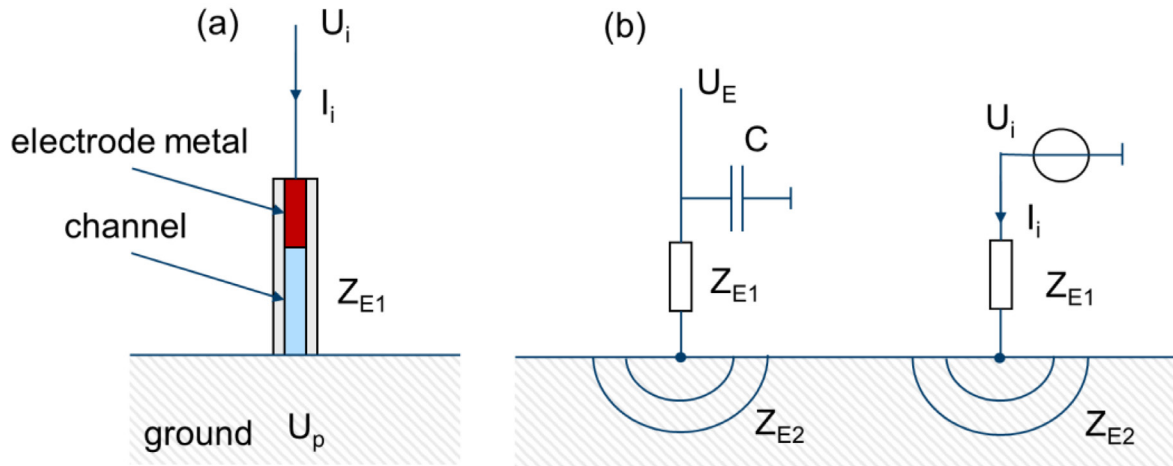$$I = I_S + \frac{1}{2}I_L. \quad (11)$$

Figure 5. Schematic diagram of the electrode contact impedances for (A) an electrode impedance measurement and (B) a potential measurement. Here, I_i is the injected current, U_p is the mean sample potential, U_i is the measured voltage at the excitation electrode, U_E is the measured voltage at the potential electrode, Z_{E1} is the channel resistance between metal and ground, Z_{E2} is the impedance of the soil and C is the capacitive load of the electrode module. Panel (A) represents the typical case for lab measurement and field measurements where the coupling is through a channel to a sample or soil and panel (B) represents the case where the electrode is inserted into the subsurface.

The bold symbols I, I_S and I_L are the corresponding current vectors. Depending on the implementation of the system of equations for the FEM calculation of all configurations, the implementation with I_{i1} and I_{i2} or the realization with I_S and I_L may be useful. The currents I_{i1} and I_{i2} are measured with the system, and the values I_S and I_L can be calculated by:

$$I_S = \frac{I_{i1} - I_{i2}}{2}$$

(12)

$$I_L = I_{i1} + I_{i2}.$$

(13)

The extended FEM model that now considers the modified source term can be written as:

$$\left[I_s + \frac{1}{2} I_L \right] = Y_G \ [U_S + U_L]$$

(14)

with

$$I_S = Y_G \ U_S$$

(15)

and

$$\frac{1}{2} I_L = Y_G \ U_L$$

(16)

where Y_G is the admittance matrix of the FEM model, and U_S and U_L are the calculated node potentials. Finally, the transfer impedances Z_G are required for data inversion. For each configuration ABMN the transfer impedances Z_G can be calculated with

$$Z_G = (U_{SM} - U_{SN})/I_{SAB} + (U_{LM} - U_{LN})/I_{SAB} = Z_S + Z_L$$

(17)

where the indices M and N denote the calculated voltages at the electrodes M and N and the indices A and B denote the injected current at the electrodes A and B. This yields the impedance Z_S for the symmetric excitation and the impedance Z_L for the leakage current excitation. The separation between Z_S and Z_L is mainly used here to illustrate the effect of capacitive coupling. In particular, the corrected spectrum

Z_C is calculated from the measured impedances Z_O to show the impact of Z_L using:

$$Z_C = Z_O - Z_L.$$

(18)

2.6. Correction of potential measurements for contact impedances

Another important measurement error in the case of EIT measurements is caused by high contact impedances of the electrodes. With respect to the potential measurement, the contact impedances Z_E together with the input capacitance C_E of the electrode modules can cause a non-negligible phase error, even if the input capacitance is only a few pF. For example, a contact impedance of 4 kΩ and a capacitance of 10 pF at 10 kHz cause an erroneous phase shift of 2.5 mrad. These errors can be corrected to a large extent with the models and methods presented in Zimmermann (2008), Kelter *et al* (2015) and Huisman *et al* (2016) for laboratory measurements on small samples and soil columns. In these cases, the electrode is coupled to the sample through a channel to avoid electrode polarization effects (see figure 5(a)) and the contact impedance Z_E between electrode and sample is largely determined by the channel impedance Z_{E1}. The contact impedance can be estimated with reasonable accuracy by measuring the voltage U_i at the electrode, the mean sample potential U_p and the current I_i through the electrode during current excitation:

$$Z_E = \frac{U_i - \text{mean}\,(U_p)}{I_i}$$

(19)

where U_p is the voltage measured at all electrodes except the current electrodes.

The method outlined above no longer applies if the electrode is inserted into the subsurface because there is no high-impedance channel that dominates the contact impedance. In principle, electrode models may be used to represent the electrodes (e.g. Boyle and Adler 2011, Rücker and Günther 2011).
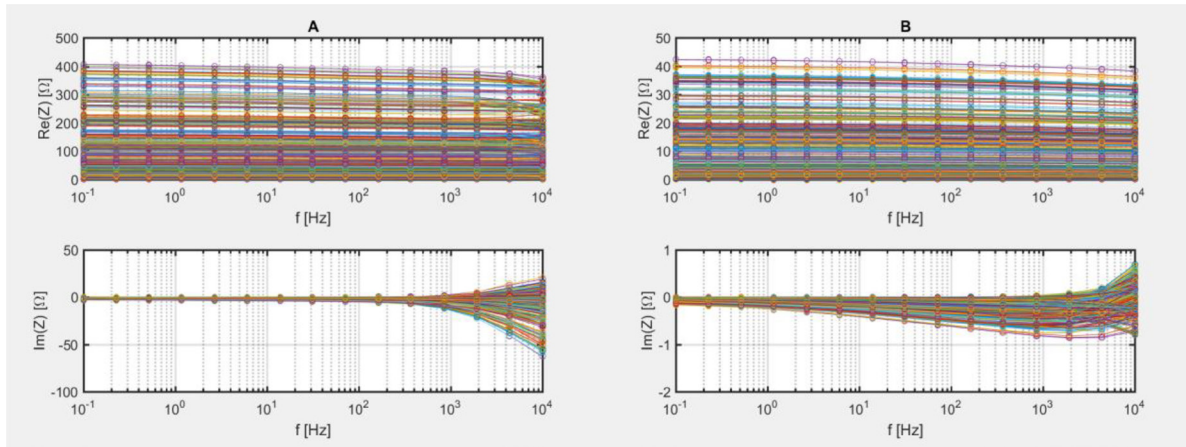
Figure 6. Impedance spectra of all configurations after standard error corrections for location *A* (left) and location *B* (right).

However, a realistic modeling of the electrode surface with respect to the correction of the measured potentials is difficult for two reasons. On the one hand, it cannot be assumed that the electrodes make contact with the sediment at all points on the surface, and on the other hand, oxide layers can strongly influence the contact impedance. Since it is currently not clear whether a complete electrode model is helpful for the correction of the potential measurements, a simpler approach is preferred here.

In this simpler approach, the electrode is represented as a point electrode in the FEM model (figure 5(b)). The impedance Z_{E1} represents the contact impedance between metal and ground, Z_{E2} the impedance of the ground and C the capacitive load of the electrode module. Assuming that Z_{E1} is much smaller than Z_{E2}, no additional correction of the phase errors in the potential measurement is necessary. It is sufficient to consider the capacitance *C* in the FEM mesh used to consider capacitive coupling because the impedance Z_{E2} is already part of the FEM model. Clearly, it would be advantageous to integrate the impedance Z_{E1} into the FEM model. In this case, the phase error could be correctly modeled and corrected for all cases. However, it is not possible to distinguish between Z_{E1} and Z_{E2} in the impedance measurement and no method is known to reliably separate these two impedances *in situ* for field measurements. Therefore, the method proposed here is only valid for the case that $Z_{E1} \ll Z_{E2}$.

2.7. Inversion of spectral electrical impedance data

It is important to realize that the consideration of capacitive coupling for the geometrically complex distribution of the cables requires a 3D FEM forward model for the reconstruction of the complex electrical conductivity distribution, whereas a 2.5D FEM model in the *x-z* plane would have been sufficient for an EIT application without correction for capacitive coupling. Since the EIT measurements do not provide information on the variability in *y*-direction, a 2D target model in the *x-z* plane was defined. In the iterative inversion process, the conductivity of this target model was assumed to be the same in *y*-direction. To invert the spectral impedance data, an

iterative Gauss–Newton procedure with Tikhonov regularization was used (Zimmermann *et al* 2008). For regularization, a second order smoothing filter is applied to the 2D plane. An error-dependent data weighting is not used for the inversion.

3. Results

The real and imaginary part of the measured impedances after standard corrections are shown in figure 6 for locations *A* and *B*. The real part of the measured impedance spectra for location *A* and *B* differed by a factor of 10 due to the different subsurface electrical conductivity. The maximum value at location *A* with low subsurface electrical conductivity was about 400 Ω. At location *B* with high subsurface electrical conductivity the maximum value was about 40 Ω. The imaginary part of the impedance spectra showed physically implausible positive values in the upper frequency range for both locations. The variation of the measured imaginary values at 10 kHz was about 100 Ω at location *A* and about 1.5 Ω at location *B*.

The real and imaginary part of the measured impedance after correction for inductive coupling is shown in figure 7. Since both sites were measured with the same cable layout and the same electrode configurations, the correction for inductive coupling was the same for both locations. The required corrections for inductive coupling ranged from $-0.9\,\Omega$ to $+1.1\,\Omega$ for the imaginary part of the measured impedance at 10 kHz. At test site *B*, the correction for inductive coupling successfully removed the physically implausible positive imaginary parts of the measured impedance at 10 kHz. The variation of the imaginary part at 10 kHz after correction was only 1.5 Ω, which is about 4% of the real part of the measured impedance (phase range). At test site *A*, the imaginary part of the measured impedance varied by about 100 Ω at 10 kHz after correction for inductive coupling, which is about 25% of the real part of the measured impedance. Despite the correction for inductive coupling, the measured spectra still showed physically implausible positive imaginary parts of the measured impedance. Of course, this was not unexpected given the broad range of values for the imaginary part of the impedance at location *A* in relation to the relatively narrow range of values required to correct for inductive coupling. These results
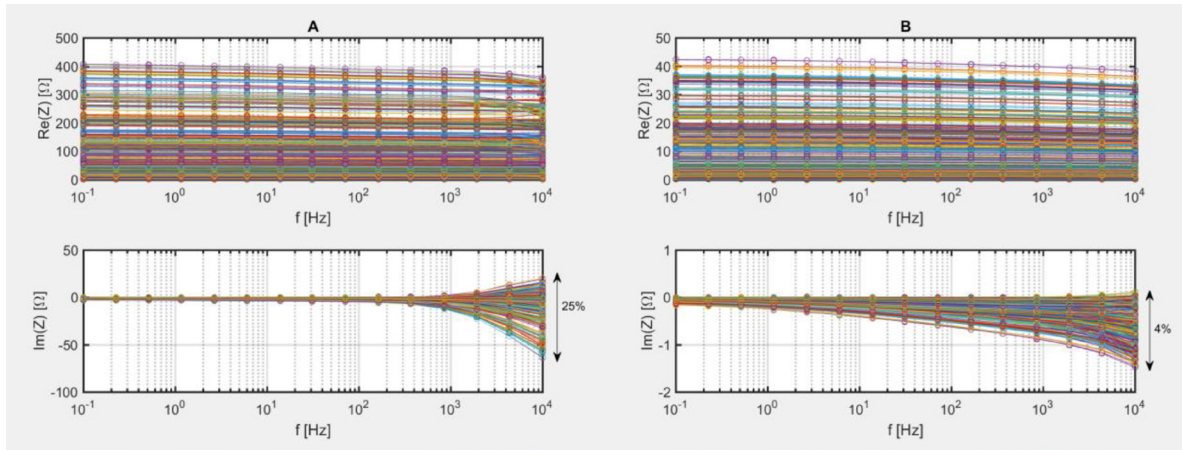
Figure 7. Impedance spectra after correction for inductive coupling for location *A* (left) and location *B* (right).
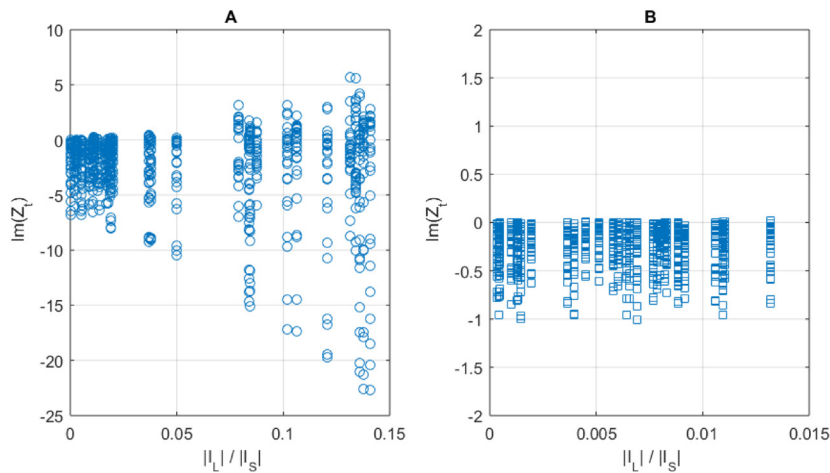

Figure 8. Imaginary part of the measured transfer impedance as a function of the normalized leakage current $|I_L|/|I_S|$ measured at 1950 Hz at location *A* and *B*.

clearly illustrate the challenges associated with surface EIT measurements at sites with low subsurface electrical conductivity that were already indicated by Kelter *et al* (2018).

In order to correct the errors due to the capacitive coupling with the extended FEM model, the total capacitances were measured at 1.2 kHz using a current excitation at each electrode for both locations *A* and *B*. The mean capacitance was 10.0 nF for location *A* and 12.5 nF for location *B*. The standard deviations of the measurements at all electrodes were 23 pF and 9 pF. Clearly, both capacitances are well within the estimated range of 9–30 nF calculated for cable to ground separations ranging from 2.5 mm to 10 mm using equation (10). This also suggests that the small difference of 2.5 nF between location *A* and *B* can be explained by a small difference (~1 mm) in mean separation between the cables and the ground surface. It also interesting to note that the contribution of the electrode modules to the measured total capacitance is negligible. The input capacitance associated with the electrode modules is approximately $29 * 10$ pF $= 290$ pF when using one current electrode and 29 potential electrodes. The contact impedances Z_E were determined as well using equation (19). They varied between 1000 and 4000 Ω for location *A* and between 300 and 600 Ω for location *B*.

After distributing the total capacitance in the 3D FEM model using the approach outlined earlier, the influence of the leakage current on the measured transfer impedance was analyzed first. For this, the imaginary part of the measured transfer impedance at 1950 Hz is plotted as a function of the normalized leakage current $|I_L|/|I_S|$ for location *A* and *B* in figure 8. For location *A* with low subsurface electrical conductivity, the imaginary part of the transfer impedances was strongly correlated with the normalized leakage current and the maximum value of the normalized leakage current is 0.3. In contrast, location *B* showed no correlation between the imaginary part of the transfer impedance and the normalized leakage current, and the maximum value of the normalized leakage current was only 0.03 (i.e. 10 times smaller than at location *A*). This clearly shows that the influence of leakage currents cannot be neglected for soils with high transfer impedances.

In a next step, the effect of considering capacitive coupling and leakage currents on the impedance spectra is shown in figure 9. For this, the measured impedances Z_O were corrected with the numerically calculated impedances Z_L that are available after data inversion using equation (18). The results show that the spread in the imaginary part of the transfer impedances
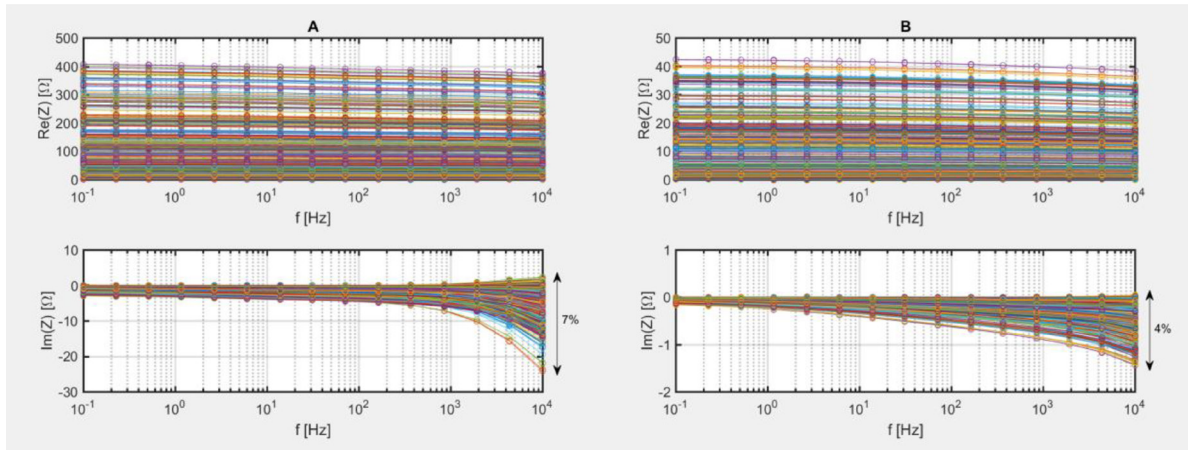
Figure 9. Impedance spectra after correction for inductive coupling and leakage currents for location *A* (left) and location *B* (right).
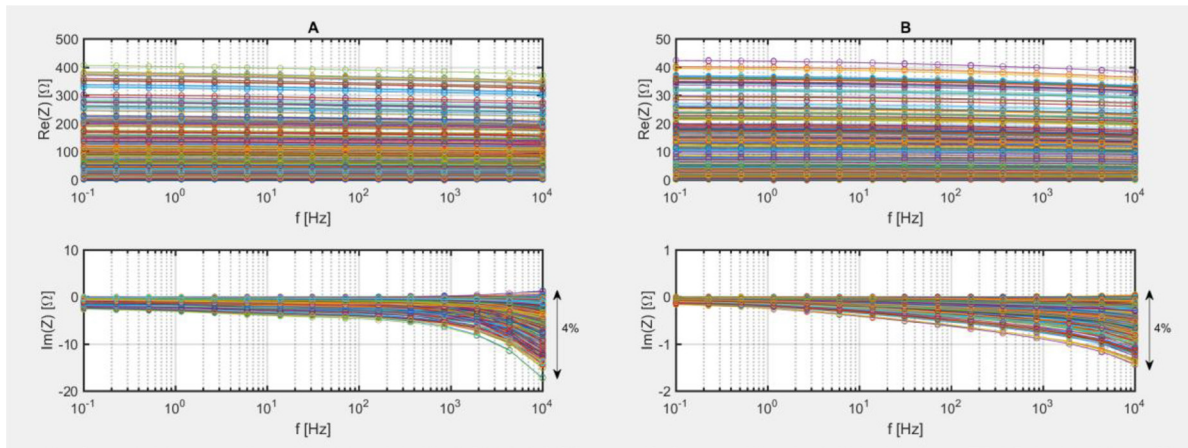

Figure 10. Impedance spectra after correction for inductive coupling, leakage currents, and the use of an additional data filter ($|I_L|/|I_S| < 0.1$) for location *A* (left) and location *B* (right).
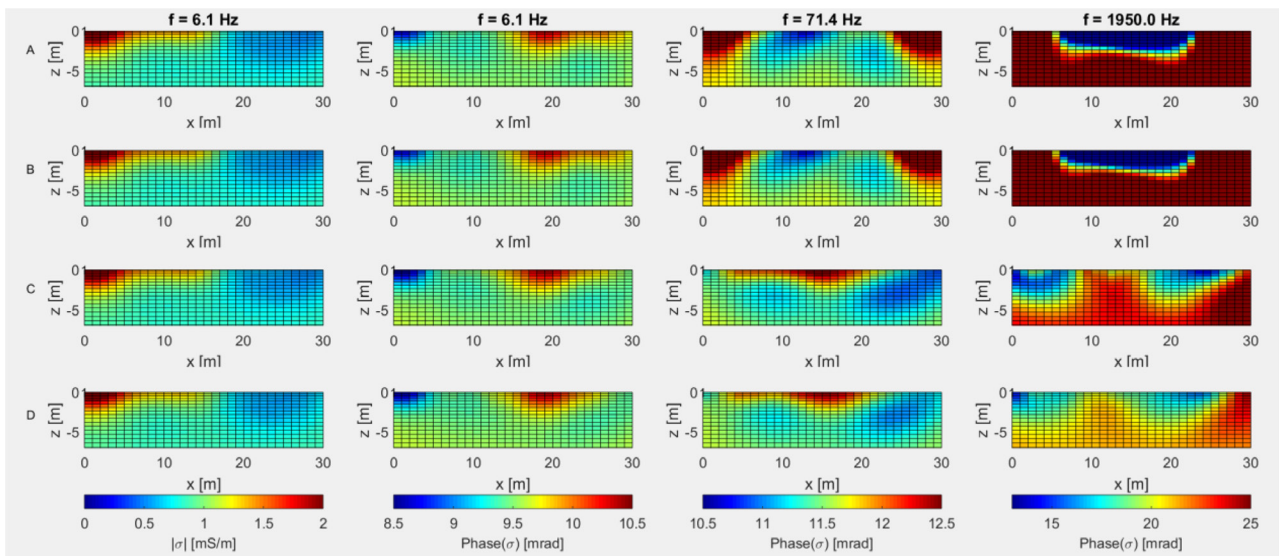

Figure 11. Magnitude and phase images of the reconstructed conductivity distribution in the *x-z* plane below the electrode row for location *A*. The indices *A* to *D* of the rows indicate different correction steps: (A) without correction, (B) with correction of inductive coupling, (C) with additional correction of capacitive coupling and (D) with additional data filter ($|I_L|/|I_S| < 0.1$). The images show from left to right the magnitude of the complex conductivity at 6.1 Hz and the phase for 6.1 Hz, 71.4 Hz, and 1950 Hz, respectively.

Figure 12. Magnitude and phase images of the reconstructed conductivity distribution in the *x-z* plane below the electrode row for location B. The indices A to D of the rows indicate different correction steps: (A) without correction, (B) with correction of inductive coupling, (C) with additional correction of capacitive coupling and (D) with additional data filter ($|I_L|/|I_S| < 0.1$). The images show from left to right the magnitude of the complex conductivity at 6.1 Hz and the phase for 6.1 Hz, 71.4 Hz, and 1950 Hz, respectively.
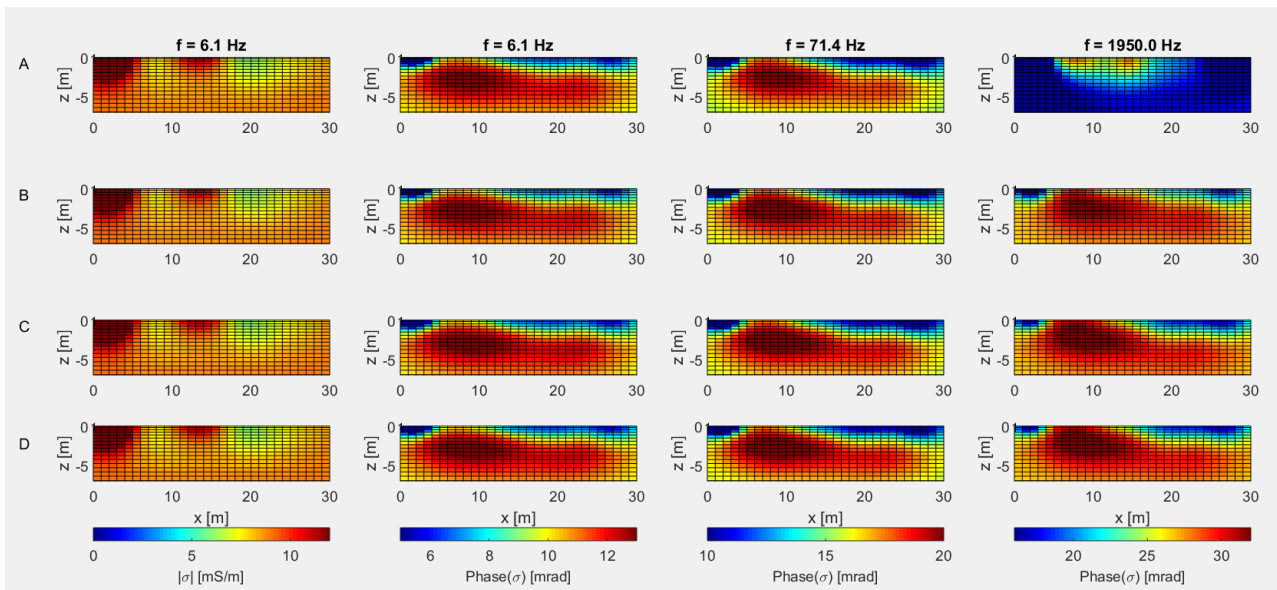
at 10 kHz was greatly reduced from 25% to 7% (phase range) for location *A* by considering capacitive coupling. However, some physically implausible positive imaginary parts of the transfer impedance remained. In contrast, only small changes were observed in the transfer impedance spectra for location *B* due to the implemented correction for capacitive coupling.

In order to remove the physically implausible transfer impedance for location *A*, a data filter was considered. For this, the normalized leakage current of the physically implausible transfer impedances was analyzed at 1950 Hz, and it was found that they were associated with measurements with $|I_L|/|I_S| > 0.1$. Therefore, these measurements were removed for all frequencies. After this last processing step, the size of dataset of location *A* was reduced from 810 to 594 transfer impedances for each frequency, but the physically implausible measurements were now also removed for location *A* (figure 10). This of course reduces the possible spatial resolution after inversion. However, no electrodes were completely excluded from the analysis due to the data filter. Before applying the filter, each electrode occurred 108 times in the 810 electrode configurations of the transfer impedances. After applying the filter, each electrode occurred at least 42 times in the remaining 594 configurations. Thus, no zones in the subsoil are completely excluded from the conductivity reconstruction.

Finally, the inversion results of the two test sites are shown for location *A* (figure 11) and location *B* (figure 12) in terms of the magnitude and the phase of the electrical conductivity. The figures show the conductivity distribution in the *x-z* plane below the electrode row. Since the magnitude is almost independent of frequency, it is shown for 6.1 Hz only. The phase of the electrical conductivity is shown for three selected frequencies (6.1 Hz, 71.4 Hz, 1950 Hz). The inversion results are presented for uncorrected data, after correction for inductive

coupling, after additional correction of capacitive coupling, and finally after applying the data filter $|I_L|/|I_S| < 0.1$. The results for both location *A* and *B* show that corrections are not required for accurate measurements of the complex electrical conductivity (magnitude and phase) at a frequency of 6.1 Hz. For the more conductive location *B*, the correction for inductive coupling improved the spectral consistency of the phase, indicating that inductive coupling was the most important source of error at this site. It can be seen that the correction for inductive coupling was considerable at 1950 Hz, but that the phase measurements at 71.4 Hz were not strongly affected yet. Corrections for capacitive coupling and data filtering did not lead to noticeable improvements in the imaged phase distribution at this location. In contrast, the imaged phase distributions at the less conductive location A were not spectrally consistent after correction for inductive coupling. Only after using the new approach to account for capacitive coupling, the spectral consistency of the imaged phase distribution improved. It can be seen that the consideration of capacitive coupling also considerably improved the phase distribution at 71.4 Hz, indicating that this relatively low frequency was already affected by the high capacitive load for this location with low subsurface electrical conductivity. The consideration of data filtering further reduced the phase values, particularly for the deeper subsurface (<3 m) at a frequency of 1950 Hz, which were found to be unrealistically high before filtering. Overall, we conclude that the proposed correction methods allow a reconstruction of the complex conductivity distribution for frequencies up to 10 kHz using surface measurements in the field. The remaining variability in phase is attributed to actual variation in the subsurface electrical properties. For example, the areas with high phase are likely associated with a higher clay fraction, but a detailed investigation of this is beyond the scope of this study.

4. Discussion and conclusions

In this paper, we have presented novel correction methods for improved reconstruction of the complex electrical conductivity distribution of the subsurface. In comparison with previous attempts to address capacitive coupling, the presented extended FEM model now also accounts for leakage currents between the soil and the cable shields. The efficiency of the new method was verified at test sites with low and high electrical soil conductivity. It could be shown that broadband field measurements with surface electrodes for frequencies up to 10 kHz are possible by using this extended FEM forward modelling. This turned out to be especially important for locations with low electrical conductivity where the effect of coupling between cable shields and soil was much stronger. In particular, the leakage current that flows from the excitation electrodes across the shields to the system ground was found to be important, and was therefore considered in the extended FEM model presented here. The estimated values of the leakage currents were additionally used for data filtering, which effectively eliminated transfer impedances with physically implausible positive phases in the upper frequency range. It is important to note that the novel correction approach presented here allows considering the coupling capacitance for all possible objects with arbitrary electrical conductivity.

A disadvantage of the proposed correction approach is the additional effort that is required to measure the leakage currents and the total capacitive load due to the cables. In addition, the extended FEM modelling approach needs to be implemented using a 3D forward model in order to consider the capacitive coupling of a fan-shaped cable layout. Instead of the fan-shaped cable layout used here, alternative cable layouts that minimize both capacitive and inductive coupling and only require a 2D forward model should be tested in future studies. Given the strength of the capacitive coupling in certain conditions, it may also be worthwhile to consider strategies to avoid capacitive coupling. This could for example be achieved by increasing the distance between cable and ground.

An important open issue is the correction of measurement errors associated with high and unequal contact impedances. Unequal contact impedances are a dominant cause for leakage currents and it is still unclear how the resulting errors can be optimally corrected in the case of high contact impedances. Another open issue for the further development of the EIT system is the current excitation. So far, a voltage source with high accuracy current measurement has been used for current excitation, as it is easier to measure the currents compared to realizing a system with an ideal current source. When using ideal current sources, the system ground initially has no reference potential. Therefore, the potential measurements would require a grounding of the system with the soil. Unfortunately, a current source with negligible capacitive coupling to the system is hardly possible due to the long electrode cables. In order to minimize leakage currents, it would however be desirable to realize an ideal current source where the two voltages at the excitation electrodes can be varied such that the leakage current is zero. Instead of the leakage current, the unbalance of the resulting voltages would then be an indicator for measurement errors. Such a development would reduce capacitive coupling, but would not avoid the need for advanced modeling of the coupling capacitances. Regardless of possible approaches for further improvement, the presented system and correction methods are a significant step forward towards an increased frequency bandwidth and improved accuracy of field EIT measurements and thus for subsurface characterization in geophysical applications.

ORCID iDs

E Zimmermann ● https://orcid.org/0000-0003-1517-6597
J A Huisman ● https://orcid.org/0000-0002-1327-0945
A Mester ● https://orcid.org/0000-0002-1587-8516
S van Waasen ● https://orcid.org/0000-0003-0682-7941

References

Bertin J and Loeb J 1976 *Experimental and Theoretical Aspects of Induced Polarization* (Berlin: Gebrüder Borntraeger)

Barber D C and Brown B H 1984 Applied potential tomography *J. Phys. E. Sci. Instrum.* **17** 723–33

Binley A and Kemna A 2005a Resistivity and induced polarization methods *Hydrogeophysics (Water Science and Technology Library)* vol 50, ed Y Rubin and S S Hubbard (Berlin: Springer) pp 129–56

Binley A, Slater L D, Fukes M and Cassiani G 2005b Relationship between spectral induced polarization and hydraulic properties of saturated and unsaturated sandstone *Water Resources Res.* **41** w12417

Börner F D, Schopper J R and Weller A 1996 Evaluation of transport and storage properties in the soil and groundwater zone from induced polarization measurements *Geophys. Prospect.* **44** 583–601

Boyle A and Adler A 2011 The impact of electrode area, contact impedance and boundary shape on EIT images *Physiol. Meas.* **32** 745

Breede K, Kemna A, Esser O, Zimmermann E, Vereecken H and Huisman J A 2012 Spectral induced polarization measurements on variably saturated sand-clay mixtures *Near Surf. Geophys.* **10** 479–89

Brown B H 2003 Electrical impedance tomography (EIT): a review *Med. Eng. Technol.* **27** 97–108

Daily W, Ramirez A, Binley A and LaBrecque D 2005 Electrical resistance tomography—theory and practice *Near Surf. Geophys.* **13** 525–50

Dahlin T, Leroux V and Nissen J 2002 Measuring techniques in induced polarisation imaging *J. Appl. Geophys.* **50** 279–98

Dahlin T and Leroux V 2012 Improvement in time-domain induced polarization data quality with multi-electrode systems by separating current and potential cables *Near Surf. Geophys.* **10** 545–65

Flores-Orozco A, Kemna A, Oberdörster C, Zschornack L, Leven C, Dietrich P and Weiss H 2012 Delineation of subsurface hydrocarbon contamination at a former hydrogenation plant using spectral induced polarization imaging *J. Contaminant Hydrol.* **136–7** 131–44

Flores-Orozco A, Velimirovic M, Tosco T, Kemna A, Sapion H, Klaas N, Sethi R and Bastiaens L 2015 Monitoring the injection of microscale zerovalent iron particles for groundwater remediation by means of complex electrical conductivity imaging *Environ. Sci. Technol.* **49** 5593–600

Flores-Orozco A, Williams K H, Long P E, Hubbard S S and Kemna A 2011 Using complex resistivity imaging to infer biogeochemical processes associated with bioremediation of an uranium-contaminated aquifer *J. Geophys. Res.* **116** G03001

Frerichs I *et al* 2017 Chest electrical impedance tomography examination, data analysis, terminology, clinical use and recommendations: consensus statement of the TRanslational EIT developmeNt stuDy group *Thorax* **72** 83–93

Holder D S 2005 *Electrical impedance tomography: Methods, History and Applications* (Bristol: IOP Publishing)

Huisman J A, Zimmermann E, Esser O, Haegel F-H, Treichel A and Vereecken H 2016 Evaluation of a novel correction procedure to remove electrode impedance effects from broadband SIP measurements *J. Appl. Geophys.* **135** 466–73

Inzoli S 2016 Experimental and statistical methods to improve the reliability of spectral induced polarization to infer litho-textural properties of alluvial sediments *PhD Thesis* Università Degli Studi Di Milano

Joyce R A, Glaser D R, Werkema D D and Atekwana E A 2012 Spectral induced polarization response to nanoparticles in a saturated sand matrix *J. Appl. Geophys.* **77** 63–71

Kelter M, Huisman J A, Zimmermann E, Kemna A and Vereecken H 2015 Quantitative imaging of spectral electrical properties of variably saturated soil columns *J. Appl. Geophys.* **123** 333–44

Kelter M, Huisman J A, Zimmermann E and Vereecken H 2018 Field evaluation of broadband spectral electrical imaging for soil and aquifer characterization *J. Appl. Geophys.* **159** 484–96

Kemna A, Binley A, Ramirez A and Daily W 2000 Complex resistivity tomography for environmental applications *Chem. Eng. J.* **77** 11–8

Kemna A *et al* 2012 An overview of the spectral induced polarization method for near-surface applications *Near Surf. Geophys.* **10** 453–68

Leonhardt S and Lachmann B 2012 Electrical impedance tomography: the holy grail of ventilation and perfusion monitoring? *Intensive Care Med.* 38 1917–29

Ozier-Lafontaine H and Bajazet T 2005 Analysis of root growth by impedance spectroscopy (EIS) *Plant Soil* **277** 299–313

Pelton W H, Rijo L and Swift C M 1978b Inversion of two-dimensional resistivity and induced-polarization data *Geophysics* **43** 788–803

Pelton W H, Ward S H, Hallof P G, Sill W R and Nelson P H 1978a Mineral discrimination and removal of inductive coupling with multifrequency IP *Geophysics* **43** 588–609

Revil A, Atekwana E, Zhang C, Jardani A and Smith S 2012a A new model for the spectral induced polarization signature of bacterial growth in porous media *Water Resour. Res.* **48** W09545

Revil A and Florsch N 2010 Determination of permeability from spectral induced polarization in granular media *Geophys. J. Int.* **181** 1480–98

Revil A, Karaoulis M, Johnson T and Kemna A 2012b Review: some low-frequency electrical methods for subsurface characterization and monitoring in hydrogeology *Hydrogeol. J.* **20** 617–58

Rücker C and Günther T 2011 The simulation of finite ERT electrodes using the complete electrode model *Geophysics* **76** F227–38

Scott J B T and Barker R D 2003 Determining pore-throat size in Permo–Triassic sandstones from low frequency electrical spectroscopy *Geophys. Res. Lett.* **20** 1450

Slater L 2007 Near surface electrical characterization of hydraulic conductivity: from petrophysical properties to aquifer geometries—a review *Surv. Geophys.* **28** 169–97

Sumner J S 1976 *Principles of Induced Polarization for Geophysical Exploration* (New York: Elsevier)

Sunde E D 1968 *Earth Conduction Effects in Transmission Systems* (New York: Dover) p 370

Telford W M, Geldart L P and Sheriff R E 1990 *Applied Geophysics* 2nd edn (Cambridge: Cambridge University Press)

Williams K H, Kemna A, Wilkins M J, Druhan J, Arntzen E, NGuessan A L, Long P E, Hubbard S S and Banfield J F 2009 Geophysical monitoring of coupled microbial and geochemical processes during stimulated subsurface bioremediation *Environ. Sci. Technol.* **43** 6717–23

Xu B and Noel M 1993 On the completeness of data sets with multielectrode systems for electrical resistivity survey *Geophys. Prospect.* **41** 791–801

York T, McCann H and Ozanyan K B 2011 Agile sensing systems for tomography *IEEE Sens. J.* **11** 3086–105

Yorkey T J, Webster J G and Tompkins W J 1987 Comparing reconstruction algorithms for electrical impedance tomography *IEEE Trans. Biomed. Eng.* **34** 843–52

Zhao Y, Zimmermann E, Huisman J A, Treichel A, Wolters B, van Waasen S and Kemna A 2013 Broadband EIT borehole measurements with high phase accuracy using numerical corrections of electromagnetic coupling effects *Meas. Sci. Technol.* **24** 085005

Zhao Y, Zimmermann E, Huisman J A, Treichel A, Wolters B, van Waasen S and Kemna A 2015 Phase correction of electromagnetic coupling effects in cross-borehole EIT measurements *Meas. Sci. Technol.* **26** 015801

Zimmermann E, Huisman J A, Kemna A, Berwix J, Glaas W, Meier H, Wolters B and Esser O 2010 Advanced electrical impedance tomography system with high phase accuracy *6th World Congress on Industrial Process Tomography (WCIPT6) (Bejing, China, 6–9 September 2010)* pp 583–91

Zimmermann E, Kemna A, Berwix J, Glaas W and Vereecken H 2008 EIT measurement system with high phase accuracy for the imaging of spectral induced polarization properties of soils and sediments *Meas. Sci. Technol.* **19** 094010